Vibrational Spectroscopy 62 (2012) 248–257

Contents lists available at SciVerse ScienceDirect

Vibrational Spectroscopy

journal homepage: www.elsevier.com/locate/vibspec

Imaging of mineral-enriched biochar by FTIR, Raman and SEM–EDX

Chee H. Chia[a], Bin Gong[b], Stephen D. Joseph[a], Christopher E. Marjo[b,*], Paul Munroe[a], Anne M. Rich[b]

[a] School of Materials Science and Engineering, University of New South Wales, Kensington, NSW 2052, Australia
[b] Solid State and Elemental Analysis Unit, Mark Wainwright Analytical Centre, University of New South Wales, Kensington, NSW 2052, Australia

ARTICLE INFO

Article history:
Received 5 March 2012
Received in revised form 15 June 2012
Accepted 15 June 2012
Available online 23 June 2012

Keywords:
Biochar
Surface analysis
FTIR imaging
Raman imaging
SEM–EDX
XPS

ABSTRACT

Recent interest in biochar characterisation has been driven by its effectiveness as a soil additive, where it can act as a carbon sink, a detoxification agent, and as a means to improve crop yields, especially when prepared as a char–mineral composite. Optimising biochar performance, raw material selection and manufacturing conditions, demands an understanding of structure and chemistry in these complex materials that typically comprise numerous minerals and organic phases. This study presents techniques to successfully image these challenging materials using Fourier transform infrared (FTIR) spectroscopy and Raman spectroscopy. The FTIR and Raman results are presented with results from scanning electron microscopy with energy dispersive X-ray spectroscopy (SEM–EDX), and X-ray photoelectron spectroscopy (XPS). We demonstrate that millimetre-scale organic phases are present in *Acacia saligna* biochar particles. Mineral enrichment of this biochar with bentonite-iron oxide generates new chemical phases, most likely through acid catalysed dehydration.

© 2012 Elsevier B.V. All rights reserved.

1. Introduction

Biochar is a carbon-rich solid material produced by heating biomass in an oxygen-limited environment and is intended to be added to soils as a means to sequester carbon and maintain or improve soil fertility and plant growth. Interactions between biochar, soil minerals and organic matter, microbes and plant roots are known to occur within a short period of time after application to the soil [1]. However, the extent, rates, and implications of these interactions are still far from being understood, and in-depth knowledge is needed for an effective evaluation of the use of biochar as a soil amendment and carbon sequestration tool. Recent studies [2–4] suggest that the types and rates of interactions (e.g., adsorption–desorption, precipitation–dissolution, redox reactions) that take place in the soil depend on the following factors: (i) feedstock composition, in particular the total percentage and specific composition of the mineral fraction (especially Fe, Ti, Mn and Ca); (ii) pyrolysis process conditions; (iii) biochar particle size; and (iv) soil properties and local environmental conditions. There is an increasing awareness of the importance of understanding the chemistry of biochar to optimise its role as a soil additive [5].

Biochar production can be performed in the presence of mineral additives to improve the bioavailability of inorganic nutrients for improved crop yields [6]. Iron plays a major role in both the stabilisation of organic carbon and uptake of nutrients by plants. Gilbert and Banfield [7] noted that nanoparticles (especially Fe and Mn oxides) can either precipitate on, or the ions can adsorb onto, the surfaces of micro-organisms forming amorphous phases. Joseph et al. [1] observed that both iron and micro-organisms can be adsorbed onto the surfaces of biochars. Nanoparticle iron that forms on the surface of biochars can catalyse the breakdown of soil organic matter [8].

Infrared spectroscopy and Raman spectroscopy are common vibrational spectroscopy techniques for investigating chemical functionality and mineralogy in biochar materials [9]. Previous applications of vibrational spectroscopy for characterisation of biochars have used Fourier transform infrared (FTIR) or Raman spectroscopic measurements of a homogenized powdered material, or point analysis of localized regions, to determine chemical character and then to relate these observations to behaviours such as crop improvement and the effectiveness of the char in CO_2 sequestration [10–13]. Previous studies where FTIR has been used to characterise biochars have focused on the changes in the biochar's functional groups as a function of pyrolysing temperature. Raman spectroscopy has also been performed as part of a number of studies of biochars, but in such studies the biochar was mixed with KBr to achieve bulk quantitative analysis [14–16]. A number of challenges must first be overcome to obtain a usable spectrum in Raman spectroscopy. The vibrational peaks tend to be masked by the presence of strong fluorescence, most likely due to the graphitic and polycyclic aromatic compounds that form during the pyrolysis. Use of longer wavelength excitation sources can assist in the reduction of fluorescence [17], however this can come at the

---

[*] Corresponding author. Tel.: +61 2 9385 4693; fax: +61 2 9385 4663.
E-mail address: c.marjo@unsw.edu.au (C.E. Marjo).

0924-2031/$ – see front matter © 2012 Elsevier B.V. All rights reserved.
http://dx.doi.org/10.1016/j.vibspec.2012.06.006

expense of localized heating and damage to the sample. However, the broad D and G bands, unique to Raman scattering, are usually strong enough to permit observation of carbon structural state formed during pyrolysis.

Infrared analysis is not affected by fluorescence and can be regarded as a powerful technique for investigating aspects of molecular chemistry in biochars. A range of different methods for performing infrared analysis have been utilized to characterise biochars: FTIR-PAS (Fourier transform mid-infrared photoacoustic) spectroscopy [12,18], where the samples are placed in a photoacoustic cell and purged with helium prior to analysis; diffuse reflectance infrared Fourier transform (DRIFT) spectroscopy in absorbance mode [11,19], where the biochar samples are mixed with KBr to form a wafer; attenuated total reflectance Fourier transform infrared (ATR-FTIR) spectroscopy [10], where the samples are in direct contact with the ATR crystal; synchrotron-based Fourier transform infrared (FTIR) spectroscopy [20] and, the most commonly used method, transmission mode FTIR, where the samples are mixed with KBr to form a pellet. When applied to a biochar surface, FTIR has been used principally to acquire point spectra. A disadvantage is that if a material is highly heterogeneous, such as biochar, this can result in sampling bias.

An infrared spectrum of biochar can be complex, often containing a variety of mineral phases, leading to an extensive variety of chemical bonds in a sample. Another significant challenge for FTIR analysis of biochars is the opacity of the sample, preventing measurements by transmission without grinding and dispersing the sample, and the low albedo, resulting in poor signal-to-noise in a reflectance FTIR measurement, even with synchrotron sources. In the case of infrared, the response from a biochar sample can be significantly improved by preparing a finely ground solid and using ATR techniques or measuring transmission of infrared light through a KBr disc, where the powdered biochar is dispersed. However, this improvement in spectral quality comes at the cost of spatial information.

Laboratory-based FTIR and Raman microscope-spectrometers are now relatively widespread and potentially enable the biochar community to better understand the distribution of chemical bonds at micron to millimetre length scales. The objective of this study is to present Raman and FTIR techniques that take advantage of the imaging capabilities of modern laboratory-based instruments to permit qualitative, spatially resolved analysis of organic functional groups and carbon structure across a significant surface area of the particle. The addition of SEM–EDX provides a comprehensive picture of the organic and inorganic chemistry on a biochar. This study includes a model application of these techniques by examining the influence of iron oxide and bentonite-iron oxide enrichment on the organic chemistry of an *Acacia saligna* biochar.

2. Experimental

2.1. Preparation of materials

Three model biochar samples were analysed using FTIR spectroscopy, Raman spectroscopy, SEM–EDX and XPS.

Sample 1: *A. saligna* woodchips were heated at 380–400 °C for 30 min in an oxygen-free environment.

Sample 2: Sample 1 was coated with iron (II) hydroxide slurry prepared as a precipitate from an aqueous solution of 0.1 M ferrous chloride and 0.1 M sodium hydroxide. The slurry coated particles were heated in an oven for 8 h at 220 °C.

Sample 3: Sample 1 was coated with iron (II) hydroxide slurry and bentonite clay prior to heating in an oven for 8 h at 220 °C.

These particular compositions were chosen as they relate to other studies performed by the authors where biochars treated in this way have been subjected to agronomic testing [6]. Further studies will include biochars treated with other mineral matter.

Samples for microscopic analysis were prepared by selecting a particle around 10–15 mm in length from each of the batches above. The particle was then mounted in epoxy resin and polished to present a relatively flat surface for analysis and marked using a scalpel to help identify the region measured using each technique. The particle was wrapped in Parafilm® prior to polishing to prevent contamination from the epoxy resin. As a result of polishing the chemistry represents a mixture of surface and subsurface regions of each sample. All sample handling was performed using gloves and clean stainless steel tools to avoid contamination.

2.2. Measurements and data analysis

Raman spectroscopy was carried out using a PerkinElmer RamanStation 400F dispersive Raman microspectrometer fitted with an echelle-based spectrograph, a 1024×256 pixel sensor array CCD detector, and a 250 mW 785 nm diode laser excitation source delivering ~100 mW at the sample when focused to its minimum 100 μm spot size. Each spectrum was collected point-by-point in a backscattered configuration from 1000 cm^{-1} to 2000 cm^{-1} using 4 cm^{-1} spectral resolution and 4×1 s exposures at each point. The images were created from a square region of 51×51 spectra for Sample 1 with a step size of 100 μm. In the case of Samples 2 and 3 a region of 25×25 spectra was measured with a step size of 200 μm. Initial data analysis was carried out using the PerkinElmer SpectrumIMAGE software to apply a baseline-offset correction to minimize intensity variations due to surface roughness. An averaged spectrum was obtained from the spectral dataset and a three-Gaussian peak fitting was performed with the Thermo GRAMS software package. All subsequent processing to generate images was performed using Matlab. The dataset was converted to ASCII-formatted subsets of the spectral region of interest from 1250 to 1675 cm^{-1} that displayed the D and G bands and the peak area estimated by summing the intensity values between 1250 and 1450 cm^{-1} (D band) and 1485 and 1675 cm^{-1} (G band). Images were generated using the ratio of D-band to G-band intensity. During image generation the peak ratio in each spectrum was allocated to 20% class intervals. The resulting relative frequency distribution provided an estimate of the area occupied by each class interval for interpretation using the *z*-axis colour scale generated by Matlab.

Infrared spectroscopy was carried out on a PerkinElmer Spotlight 400 FTIR microspectrometer fitted with a liquid nitrogen-cooled, 16-element linear array mercury cadmium telluride (MCT) detector. Two methods were used to collect FTIR images; ATR imaging and reflectance imaging. The use of ATR imaging using a germanium crystal resulted in inconsistent contact across the sample, as well as damage to the brittle sample surface. The resulting intensity artefacts masked the chemical distribution across the sample. The preferred method was reflectance FTIR imaging since, as a non-contact measurement, there was no damage to the sample surface, a larger region could be analysed, and the spectra were acceptable for image generation. All FTIR spectra were collected in the mid-infrared from 4000 cm^{-1} to 650 cm^{-1} using 16 cm^{-1} spectral resolution and 64 accumulations for each collection by the array. A 16 cm^{-1} spectral resolution provided sufficient chemical information at each point to enable image generation, while allowing measurement of a significant area of the particle surface within 3 h. The images comprised 100×100 spectra using a 50 μm step size. The data was pre-processed using the PerkinElmer SpectrumIMAGE software to perform an atmospheric correction to remove the influence of carbon dioxide and water in the beampath (supporting information, Fig. S1).

Principal component analysis (PCA) of vibrational spectra can be an effective tool in vibrational spectroscopic imaging to rapidly

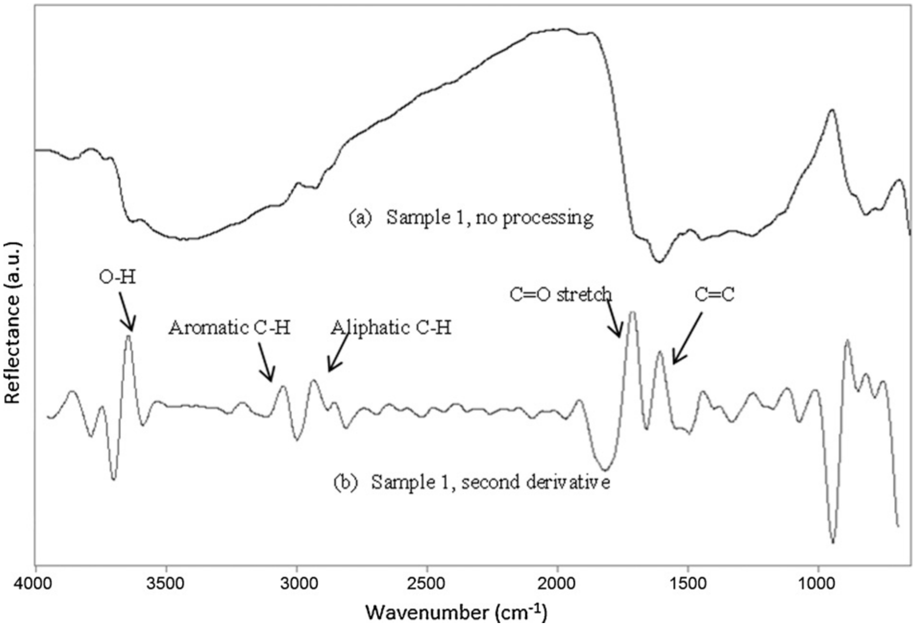

Fig. 1. Averaged FTIR spectrum of Sample 1, (a) unprocessed absorption spectrum and (b) second-derivative of spectrum. Spectra are scaled and offset for clarity.

survey phases present in a sample [21]. The FTIR data for all three samples was analysed using PCA and a score image was produced to indicate the relative prevalence of each factor (supporting information, Fig. S2(a)–(c)). PCA is particularly useful as a survey technique to establish the number of chemical phases present on biochar and their distribution, and serves as a useful first step prior to analysis using second-derivative peak heights. Identifying the chemical bonds localized in each phase was found to be quite difficult using PCA factors or evaluating individual spectra from each phase (supporting information, Fig. S2(d) and (e)). Images created from second-derivative peak heights were more useful in this regard.

Following PCA the FTIR data was re-analysed by calculating the second-derivative using a 13-point Savitzky–Golay procedure [22]. The SpectrumIMAGE software was used to generate a peak height intensity image for each of the wavenumbers in the spectrum. In cases where the phases match those observed in the PCA score plots, the peak position was noted and the subsequent data analysis was performed using Matlab. The dataset of 10,000 spectra was converted to ASCII-formatted subsets of the spectral region of interest. Images were generated from the peak height for each bond vibration. The peak height was allocated to 20% class intervals during image generation. The resulting relative frequency distribution provided an estimate of the sample area occupied by each class interval for interpretation using the *z*-axis colour scale generated by Matlab. In the case of Sample 2, the measured region comprised biochar and a noisy unfocussed region off the edge of the sample. The non-sample region was easily distinguished from the biochar as it displayed random noise in the second-derivative image and these spectra were identified and set to a peak height equivalent to 0% when generating the images.

XPS analysis was performed on a Thermo Scientific ESCALAB250Xi using a 500 μm diameter beam of monochromatic Al Kα radiation (photon energy = 1486.6 eV) at a pass energy of 20 eV. The core level binding energies (BEs) were aligned with respect to the C 1s BE of 285.0 eV.

Scanning electron microscopy with energy dispersive X-ray spectroscopy (SEM–EDX) was carried out on a Hitachi S3400 SEM operating at 15 kV with a probe current of 0.6 nA to which a Bruker silicon drift detector EDS system had been interfaced. SEM–EDX was the final step in the analysis of each sample as they required sputtered coating with chromium prior to analysis.

Optical microscopy was performed using a Leica M165C microscope with cold light source illumination directed at approximately 45° above the surface of the sample.

3. Results and discussion

Three model biochar samples were designed for this study. Sample 1 was an unmodified *A. saligna* biochar prepared at 380–400 °C for 30 min in an oxygen-free environment. This sample was expected to be the least chemically complex and, thus, suitable to develop the experimental methodology and data processing for all three samples. Sample 2, with added iron (II), and Sample 3, with added iron (II) and bentonite, represent two types of mineral-enriched biochar. FTIR and Raman imaging were used to examine the distribution of chemical bonds across the sample and related to the elemental distributions observed in SEM–EDX.

3.1. Sample 1: non-enriched biochar

The reflectance FTIR of Sample 1 was measured using 50 μm steps across a surface region of 5000 μm × 5000 μm to create 10,000 spectra. Fig. 1(a) shows the averaged spectrum from the imaged region. The spectrum exhibits strong baseline effects that make it difficult to observe the small peaks from the chemical bonds on the sample. The peak intensities for an individual spectrum in the image were very weak and typically ranged from 1% to 2% transmission.

In the presence of a highly variable baseline, the conversion of the spectra to the second-derivative is an effective technique to obtain useful chemical information from a sample [21]. The second-derivative spectrum in Fig. 1(b) reveals small peaks superimposed on the broader baseline peaks that dominated the unprocessed spectrum. Previously overlapped peaks appear separated since the second-derivative enhances subtle changes in curvature due to peak overlap that can mask important chemical information about the sample. The presence of O—H, C—H, C═O, C═C and numerous single-bond stretches can be observed.

Table 1
XPS results for Samples 1–3, showing at.% for all elements detected as well as the relative at.% for the C 1s peak corresponding to different organic functional groups. Column one lists the element along with the relevant atomic orbital from which the photoelectron originated.

Transition	Abundance (at.%)			Relative C 1s distribution (at.%)		
	Sample 1	Sample 2	Sample 3	Sample 1	Sample 2	Sample 3
Al 2p						
A			2.96			
C 1s						
C—C/C—H	60.72	26.49	43.20	79.9	69.2	71.9
C—O groups	10.11	7.45	11.08	13.3	19.5	18.4
C═O groups	3.00	1.66	3.45	4.0	4.3	5.7
O═C—O groups	2.16	2.70	2.39	2.8	7.1	4.0
Ca $2p^3$			0.32			
Cl $2p^3$						
A		0.38				
B		0.2				
Fe $2p^3$		13.86	0.13			
Mg 1s		1.65				
N 1s						
A	1.74	0.61	0.32			
B			0.26			
Na 1s		0.95	0.16			
O 1s	16.6	42.22	27.86			
Si 2p	4.47		7.87			
Si 2s		1.14				

Sample 1 was found to comprise four major elements by ultimate analysis (performed by Bureau Veritas International Trade Pty Ltd. in Australia using the relevant Australian standard, AS1038.6.1): carbon (75.0%), oxygen (20.7%), hydrogen (3.6%), and nitrogen (0.7%). The ultimate analysis is in good agreement with the XPS analysis (Table 1). As there are only three major elements (C, H, and O), there are a limited number of bond vibrations that can be assigned to peaks in the FTIR. Wood cellulose is a polymer rich in hydroxide groups, and even after pyrolysis some hydroxide, and possibly water, remains in the sample, hence the peak at 3640 cm^{-1} could be assigned to OH stretching, although mineral based Si—OH could be expected as well (Fig. 1). An aliphatic C—H stretch is observed at 2920 cm^{-1}, confirming that the cellulose is not entirely carbonized during pyrolysis. The aromatic C—H stretching at 3050 cm^{-1} matches the value expected from lignin aromatic residues, but a contribution from the aromatization of cellulose residues during pyrolysis would be expected. A broad unsymmetrical peak with a maxima at 1744 cm^{-1} is due to C═O stretching. This peak comprises a variety of C═O containing functional groups, including ketones, carboxylic acids esters, and anhydrides. The band at 1605 cm^{-1} can be assigned to C═C bond stretching derived from aromatic rings in the lignin, as well as newly aromatized and carbonized material from carbohydrate ring dehydration and cyclisation during pyrolysis. Peaks expected from single bond stretching, and other deformation bands in the region 1500 to 650 cm^{-1} are also observed. These are numerous and overlapped, and difficult to assign in the averaged spectrum.

The averaged Raman spectrum of Sample 1 from 1000 to 1700 cm^{-1} is shown in Fig. 2. Raman spectroscopy of biochar is clearly most effective for analysis of D and G bands typically found at 1350 cm^{-1} and 1580 cm^{-1} respectively, and are evidence of polyaromatic hydrocarbons and graphitic material [23]. The G-band represents vibrations of sp^2 carbon atoms found in graphitic materials and double bonds, while the D-band is linked to the breathing modes of disordered graphite rings [24]. The 1000–1750 cm^{-1} region in Fig. 2 could be fitted using three Gaussian functions and a linear baseline to achieve an adequate match to the experimental data (supporting information, Table S1). The peaks at 1192 cm^{-1} and 1360 cm^{-1} were assigned as D-band peaks, and the peak at 1578 cm^{-1} assigned to the G-band. The D-band peaks are significantly stronger than the G-band with a D/G peak area ratio of 11.5 indicating that most of the graphitic carbon is disordered.

Fig. 3 shows SEM images, FTIR, and Raman images for Sample 1. The SEM image (Fig. 3(a)) shows the remains of the vessel structure retained from the *A. saligna* wood, overlaid by smooth striations running diagonally from the top left to the bottom right. A magnified SEM image of one striation is shown in Fig. 3(b), and shows a relatively flat surface alongside the vessel structure that makes up the bulk of the sample. Fig. 3(c) is an image generated from the second-derivative FTIR data. The image shows height variation of a peak at 2080 cm^{-1} across the sample. Those portions of the image coloured yellow–orange–red represent the strongest peak intensity (60–100%) of the observed intensity range. This strong peak intensity makes up 5% of the measured area of Sample 1 and appears to correspond with the striations seen in the SEM (Table 2).

The FTIR image in Fig. 3(d) is generated from the 2920 cm^{-1} second-derivative peak intensity representing C—H stretching. The distribution of C—H peak intensity shows an inverse relationship to that seen in Fig. 3(c) for the peak at 2080 cm^{-1}. The striations are areas of lower C—H intensity, while the bulk of the sample has

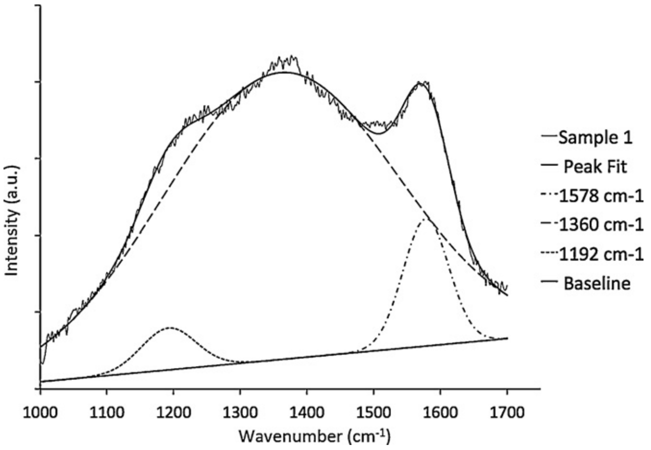

Fig. 2. Averaged Raman spectrum of Sample 1 showing three-Gaussian peak fit for D2 and D1-bands (1192 cm^{-1} and 1360 cm^{-1}), and the G-band (1578 cm^{-1}).

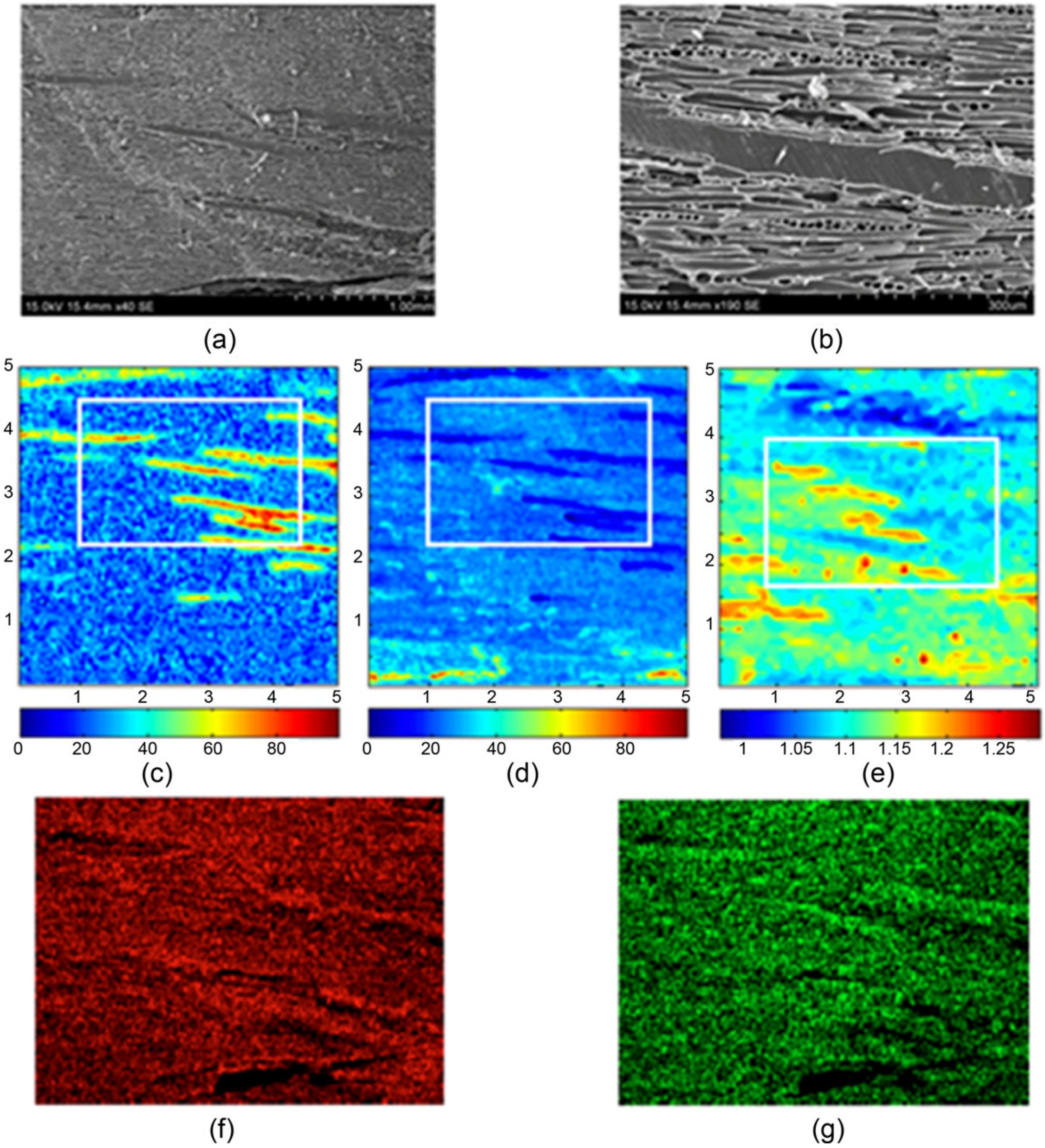

Fig. 3. Sample 1 SEM image (a) and higher magnification image (b) of one striation. Reflectance FTIR images of Sample 1 (c) %intensity at 2080 cm^{-1} (d) %intensity 2920 cm^{-1} (e) D/G peak ratio. The region indicated by the white box on images c, d and e indicates the location of the SEM image (a). Dimensions on the FTIR images are in mm. SEM–EDX Kα maps of (f) carbon and (g) oxygen from the region denoted by the white box. (For interpretation of the references to color in this figure legend, the reader is referred to the web version of this article.)

higher C—H intensity. The likely reason for lower C—H intensity within the striation phase is more extensive ring formation and dehydration converting aliphatic organic material (C—H rich) to aromatic organic material (C—H poor).

The striations in Sample 1 are clearly a different chemical phase from the bulk region, and are not simply the result of intensity variations due to focusing on a rough sample. The same features consistently appear when generating a FTIR second-derivative intensity image of a number of peaks including 3640, 1888, 1063 and 856 cm^{-1} (supporting information, Figs. S1 and S3).

Most of the FTIR peaks giving rise to the striation features are from organic functional groups commonly observed in biochar. The peak at 3640 cm^{-1} would be expected from organic OH stretching, with contributions from any water that may have been retained in the sample as well as any mineral-derived Si—OH groups. The aromatic groups in the sample give rise to C=C stretching at 1605 cm^{-1} and aromatic C—H deformation modes at 856 cm^{-1}. The peak at 1063 cm^{-1} can be assigned to stretching from varieties of C—O bonds in ethers, esters and carbonates. However, the peaks at 2080 and 1888 cm^{-1} are notable as this region is normally silent in the FTIR for most organic compounds and polymers. XPS analysis (Table 1) shows the presence of 1 at.% nitrogen, and this would support the possibility of the 2080 cm^{-1} peak arising from an organic azide group (—N=N=N) or a ketene group (>C=C=O). The poor stability of azides at the high temperature required for pyrolysis suggests that a ketene may be a more likely candidate for this peak. The peak at 1888 cm^{-1} could be tentatively assigned to the C=O stretch of a cyclic acid anhydride ring C=O. Other possibilities for this peak, such as acid halides, and amine or imine hydrohalide salts would seem to be precluded due to the absence of halogens in the XPS analysis. The formation of cyclic anhydrides by thermal dehydration of polycarboxylic acids has good precedence in the

Table 2
A summary of the main FTIR chemical bond vibrations used to generate FTIR images for Samples 1–3. Selection was based on FTIR peaks that revealed non-random phases of strong and weak-intensity. The terms “weak-intensity” and “strong-intensity” typically refer to second-derivative peak heights between 0–40% and 60–100% respectively. A subset of representative images is presented in the text and supporting data.

Chemical bond (functional group)	Sample 1 FTIR peak position Feature: intensity	Sample 2 FTIR peak position Feature: intensity	Sample 3 FTIR peak position Feature: intensity
O—H stretch (Si—OH)	3640 cm^{-1} Striations: strong	3640 cm^{-1} Striation: strong Iron region: weak	3640 cm^{-1} Clay regions: strong
C—H stretch (alkyl CH)	2920 cm^{-1} Striations: weak	2952 cm^{-1} Striation: strong	Peak not observed No features observed
C═O stretch (ketene C═C═O)	2080 cm^{-1} Striations: strong	Peak not observed	Peak not observed No features observed
C═O stretch (cyclic anhydrides)	1888 cm^{-1} Striations: strong	Peak not observed	1864 cm^{-1} Clay regions: strong Vessel pores: weak
C═O stretch (ketones, carboxylic acids)	1744 cm^{-1} Striations: strong	1744 cm^{-1} Striation: strong Iron region: weak	1752 cm^{-1} Clay regions: weak Vessel pores: strong
C═C stretch (aryl, double-bond)	1605 cm^{-1} Striations: strong	1605 cm^{-1} Striation: strong Iron region: strong	1605 cm^{-1} No features observed
Si—O stretch (Si—O—Si)	1104 cm^{-1} No features observed	1104 cm^{-1} Striation: not observed Iron region: strong	1104 cm^{-1} Clay regions: strong
C—O stretch (alkyl/aryl ethers)	1063 cm^{-1} Striations: strong	1032 cm^{-1} Striation: not observed Iron region: weak	Peak not observed No features observed
Si—O stretch (Si—O—Si)	952 cm^{-1} Striations: strong	952 cm^{-1} No features observed	952 cm^{-1} Clay regions: strong
C—H stretch (CH deformation)	856 cm^{-1} Striations: strong	832 cm^{-1} Striations: strong Iron region: not observed	832 cm^{-1} No features observed

literature [25], as does thermal dehydration of a carboxylic acid to a ketene [26].

Fig. 3(e) is an image generated using the ratio of areas of the Raman D and G regions of Sample 1. The regions with $D/G > 1.15$ (yellow–orange–red) have a similar size and orientation to the striations on the SEM micrograph and occupies around 8% of the measured surface of Sample 1, which is comparable to the FTIR image in Fig. 3(c) where the striations occupy 5%. These high D/G ratio regions represent areas with relatively high sp^2 carbon disorder compared to the bulk of the sample.

The elemental distribution of carbon and oxygen in Sample 1 was probed using SEM–EDX to measure the intensity of the Kα line across the sample (Fig. 3(f) and (g)). Both elemental images show a low-intensity feature that matches a crack at the bottom of the SEM image, and the oxygen map shows some slightly higher intensity regions that coincide with the striations identified in both the SEM micrographs and FTIR maps.

3.2. *Sample 2: iron (II)-enriched model*

Sample 2 was a model of iron-enriched biochar prepared by coating Sample 1 with iron (II) hydroxide slurry and heating in an oven for 8 h at 220 °C. The addition of iron to biochar changes the FTIR spectrum; the striations observed in Sample 1 are not observed and additional FTIR peaks are found. One possibility for the absence of striation features seen in Sample 1 is rapid hydrolysis of the reactive ketenes and cyclic anhydrides to carboxylic acids on addition of the aqueous iron hydroxide slurry. However, it should be noted that the absence of the striation features might also result from structural variation expected from a range of naturally derived particles.

A SEM image of the Fe-enriched sample is shown in Fig. 4(a) with two areas of interest labelled as point 1 and 2. A higher magnification image of iron-mineral particles adhering to the surface of the biochar at point 1 is shown in Fig. 4(b). The presence of iron on this sample is clearly shown in the SEM–EDX map in Fig. 4(c) where the iron distribution (green) is overlaid on the carbon distribution (red). From this image it can be seen that the highest concentration of iron is at point 1, the lower left edge of the particle, with much lower concentrations of iron across the rest of the biochar surface. The image in Fig. 4(d) was generated from FTIR peak height of the second-derivative peak at 1104 cm^{-1}. The region corresponding to point 1 shows a high-intensity region (80–100%) matching the iron distribution observed in the EDX map in Fig. 4(c). The iron on this sample was applied as iron hydroxide prepared from ferrous chloride, so the majority of the iron is expected to be ferric and ferrous oxides formed during the 8 h heating process at 220 °C. However iron (II) and iron (III) oxides absorb below 600 cm^{-1} in the infrared [27] so the peak at 1104 cm^{-1} cannot be attributed to iron oxides on the sample. The presence of 1 at.% of silica in the XPS analysis suggests that the 1104 cm^{-1} peak is due to a bridging Si—O—Si stretch found in silicate glasses [28] associated with the iron oxide deposits, possibly present as an impurity in the iron hydroxide slurry.

Fig. 4(e) and (f) is FTIR intensity images of the C—H stretch at 2952 cm^{-1} and the C═O stretch at 1744 cm^{-1}, respectively. A small high-intensity feature (80–100%) at point 2 is observed from these two peaks. The area around point 2 shows a higher relative proportion of C═O and CH groups formed from uneven dehydration or oxidation of the surface during the oven-drying process. This feature can also be identified in images created from C═C stretching and aromatic C—H deformation modes (supporting information, Fig. S4(c) and (d)). A notable feature in the 1744 cm^{-1} image, Fig. 4(f), is the low-intensity feature at point 1. The reduction in C═O intensity indicates that the layer of iron oxides is masking the organic surface from additional chemical reactions that are taking place across the rest of the surface. Iron oxide is transparent in this region of the infrared, so the decrease in C═O intensity cannot be due to preferential absorption of the incident infrared by the iron oxide layer. The importance of the heating process in facilitating oxidative/pyrolytic processes was demonstrated in a control

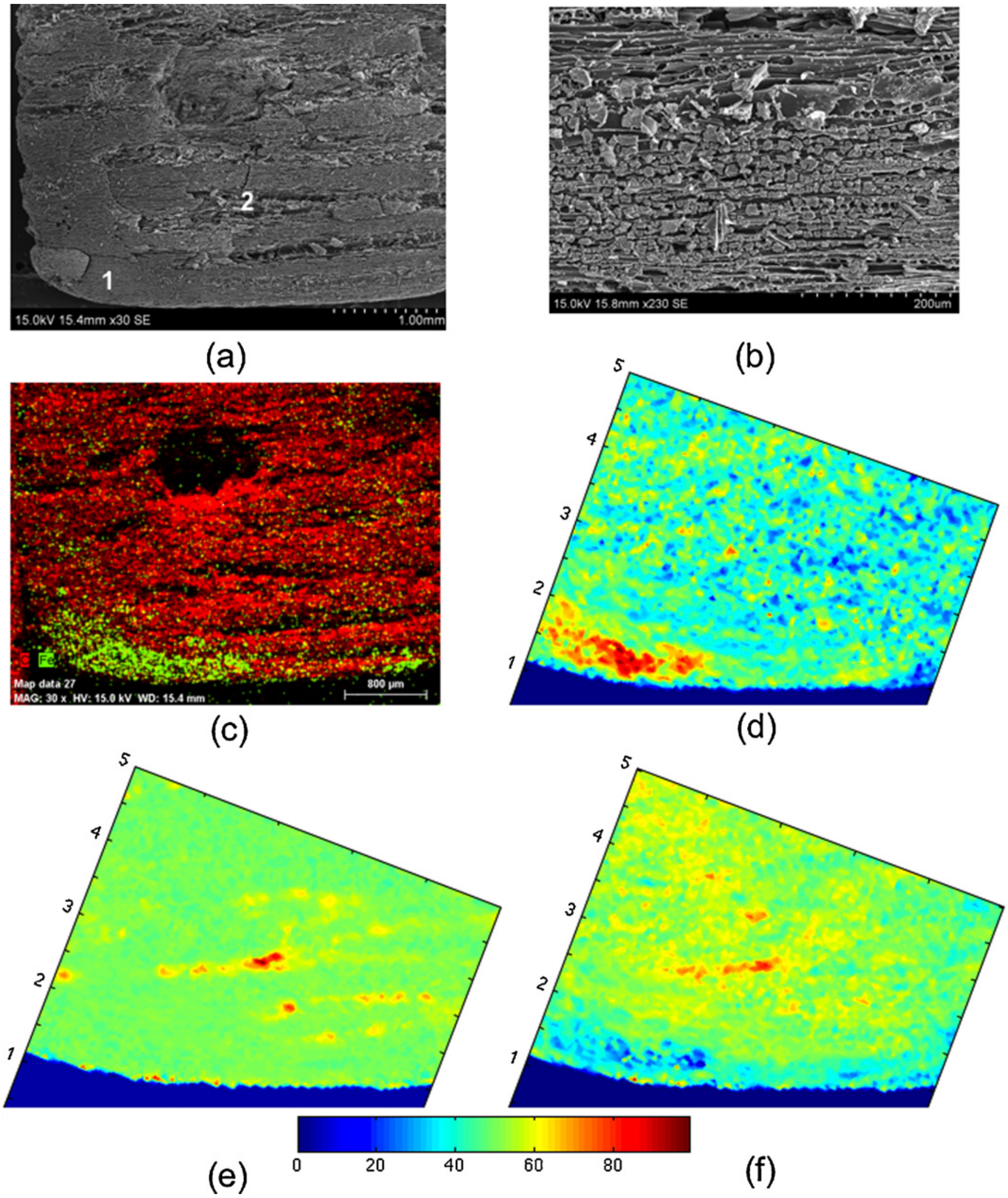

Fig. 4. Sample 2 SEM image (a) showing two notable regions. (b) SEM expansion of iron particles observed in region 1. (c) SEM–EDX elemental map of iron (green) overlaid on carbon (red). Reflectance FTIR images of Sample 2 (d) %intensity at 1104 cm^{-1}, (e) %intensity 2952 cm^{-1} and (f) %intensity 1744 cm^{-1}. Dimensions on the FTIR images (d and e) are in mm and colour scale indicates percentages. (For interpretation of the references to color in this figure legend, the reader is referred to the web version of this article.)

sample prepared by soaking in water, then oven-drying at 220 °C for 8 h. Oven drying resulting in clear changes in the organic functional groups, particularly the C=O stretching (supporting information, Fig. S5).

The average Raman D–G ratio decreases compared to Sample 1 during the oven drying (supporting information, Fig. S6 and Table S1). However unlike Sample 1, the Raman features do not match the EDX and FTIR features at points 1 or 2. It appears that the phases observed in the Raman D–G image develop independently of the iron distribution across the sample.

3.3. Sample 3: iron (II)-bentonite enriched model

Sample 3 was a model for iron–clay enrichment prepared by coating Sample 1 with slurry of iron (II) hydroxide and bentonite clay and heating for 8 h at 220 °C. Fig. 5(a) is an optical micrograph of a biochar particle with a white box indicating the region imaged using reflectance FTIR. This region has been expanded for clarity in Fig. 5(b). Points 1–4 are examples of areas where inorganic deposits have adhered to the biochar surface. The microscope images show that the measured surface is across the end-grain region of the original wood particle. Compared to electron microscopy, the use of white light illumination has the advantage of revealing red-coloured areas (points 1, 2 and 4) that are probably clays enriched with iron oxides, and white areas (for example point 3) that may be iron-poor bentonite clay regions.

The reflectance FTIR images in Fig. 5(c–f) show the distribution of the second-derivative peak height across the sample, and converted to percentages on the colour scale. The striations observed on Sample 1 were not observed on Sample 3. As with Sample 2, the highly reactive groups in this phase would have been hydrolysed to carboxylic acids immediately on addition of an aqueous slurry,

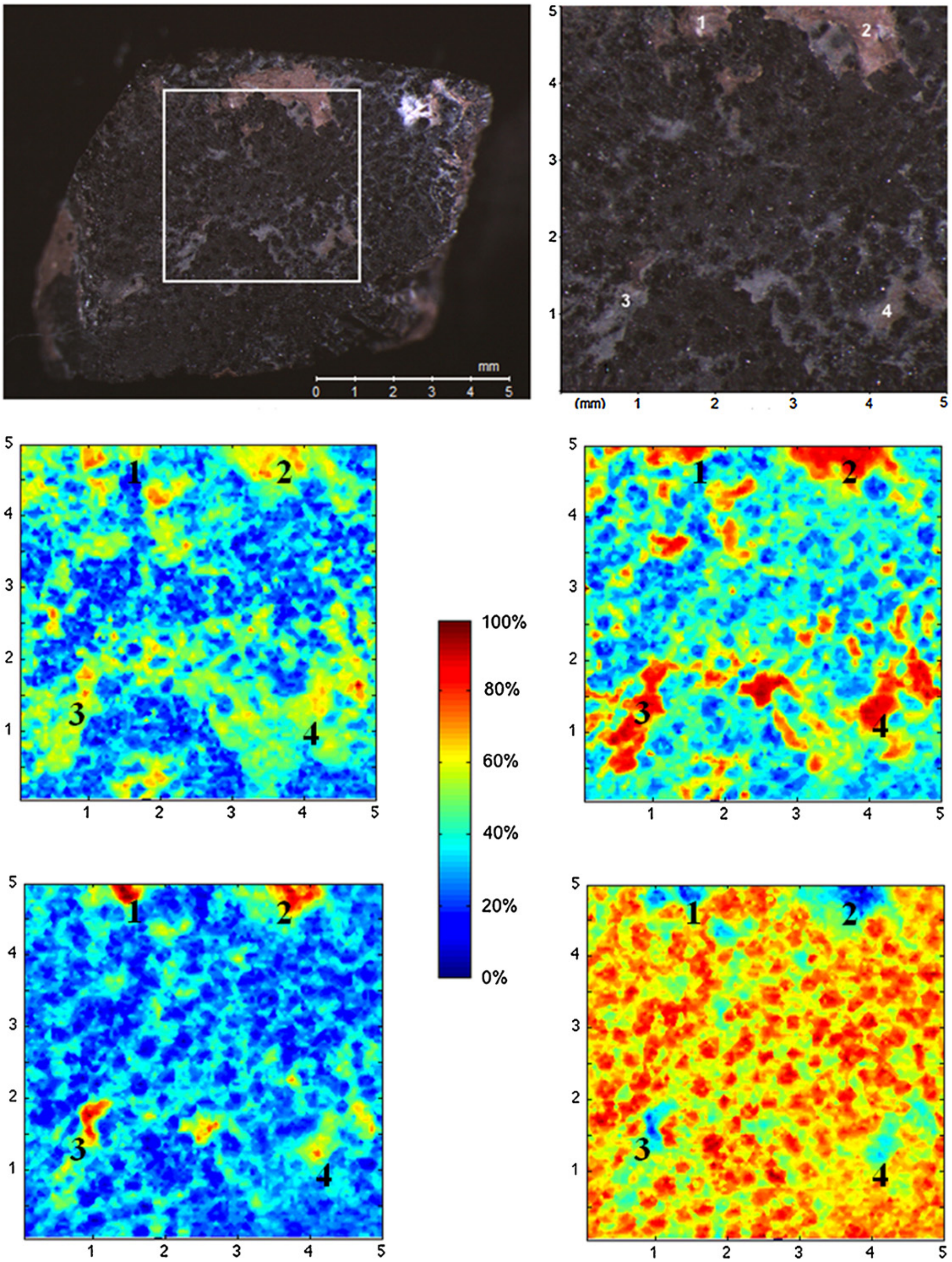

Fig. 5. Sample 3 Optical microscope image (a) with a white box indicating the region imaged using FTIR. This region has been expanded in (b) and is labelled with four points where mineral deposition can be observed. Reflectance FTIR images (dimensions in mm) are shown in (c) %intensity at 1104 cm^{-1}, (d) %intensity 952 cm^{-1}, (e) %intensity 1864 cm^{-1}, and (f) %intensity 1752 cm^{-1}.

although it is also possible that these regions may not be observed at the end-grain region of a particle, or simply not present due to natural structural variation. However, new phases were observed that correspond to the inorganic deposits at points 1–4 shown in the optical microscopy images. Fig. 5(c) and (d) are images from the 1104 cm^{-1} and 952 cm^{-1} FTIR peaks, respectively. These two peaks can be assigned to transverse optical (TO) stretching vibrations with different Si—O—Si geometries [28] in silicate and aluminosilicate minerals in the clay–iron oxide mixture applied to the biochar. The 952 cm^{-1} image (d) is particularly effective at revealing the correspondence of Si—O stretching in the red and white mineral deposits observed in the micrograph (b).

Fig. 5(e) and (f) shows images from the 1864 cm^{-1} and 1752 cm^{-1} peaks respectively. A visual comparison of the two images shows an inverse relationship, where points 1–4 are observed as high-intensity regions in image (e) (1864 cm^{-1} peak), but low-intensity regions in image (f) (1752 cm^{-1} peak). The area analysis of the images confirms this inverse relationship;

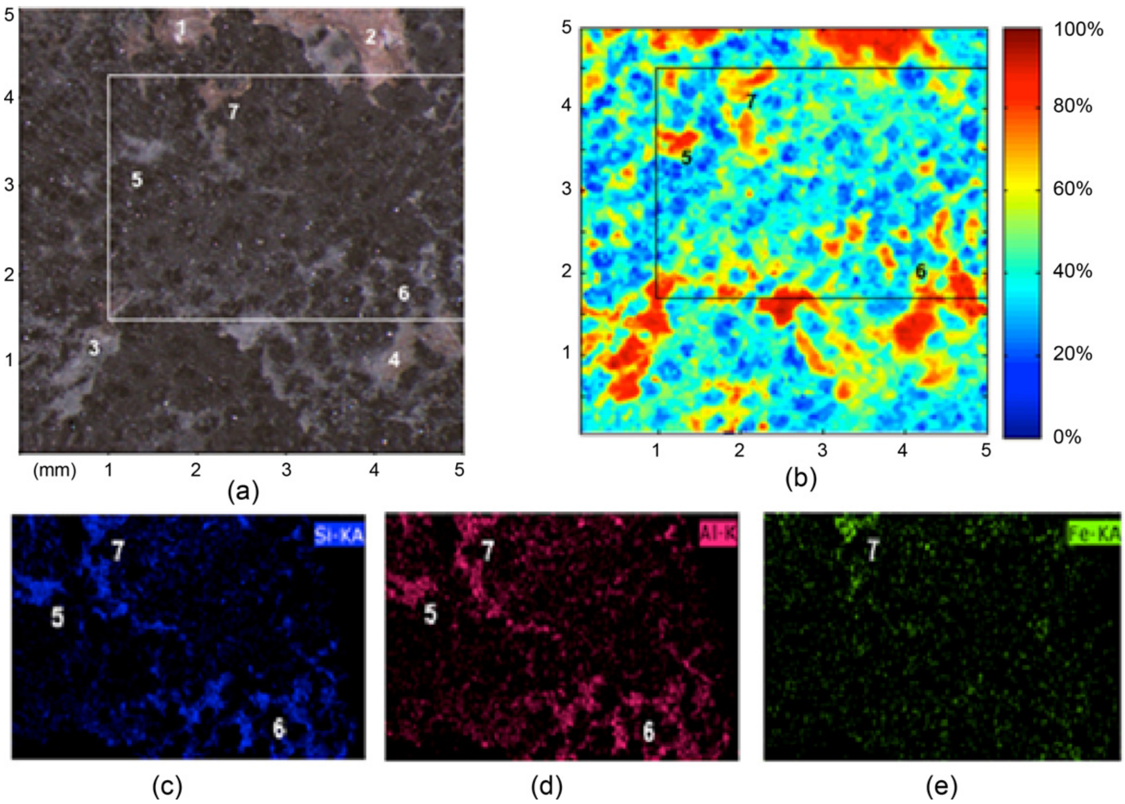

Fig. 6. Sample 3 (a) Optical microscope image with a white box indicating the region imaged using SEM–EDX. (b) Reflectance FTIR image showing %intensity at 1104 cm^{-1} and black box indicating the region images using SEM–EDX (dimensions in mm). SEM–EDX maps shown for (c) silicon, (d) aluminium, and (e) iron distribution across the sample.

high-intensity peaks (60–100%) in image (e) occupy 2.5% while low-intensity peaks (0–40%) occupy 2.9% of image (f). It was hypothesized that this observation is the conversion of a chemical bond with a peak at 1752 cm^{-1} to a bond with a peak at 1864 cm^{-1}, owing to the presence of the overlying mineral layer. The 1752 cm^{-1} peak is typical for C=O stretching found in ketones and carboxylic acid derivatives and has a high-intensity over most of the surface of the biochar in image (f). It was proposed that Lewis acidic aluminium or protic acid volatiles in the clay [29] at points 1–4 facilitate cyclic dehydration of neighbouring carboxylic acids to form a cyclic carboxylic acid anhydride with a C=O peak at 1864 cm^{-1}. The result is image (e) where the cyclic anhydride stretch shows a strong intensity where the bentonite deposits are observed. Strong OH stretching (3640 cm^{-1}) is seen at points 3 and 4 (supporting information Fig. S7(c)) presumably due to terminal Si—OH groups in the bentonite.

Another notable observation from Fig. 5(f) is the chemical visualization of the vessel pores. These features show highest intensity for ketone/carboxylic C=O stretching and may arise from the localization of lignin between the cellulose and hemicellulose components that make up the vessel walls in the original wood, and these components would react differently during pyrolysis.

Fig. 6 reproduces the optical microscope image of Sample 3 (a) and the FTIR image generated from the intensity of the 952 cm^{-1} Si—O stretch (b). The boxes within each image indicate the samples areas that relate to the EDX elemental maps below, along with three points 5, 6 and 7 where mineral phases are observed. The EDX maps show the distribution of (c) silicon, (d) aluminium and (e) iron. The distribution of silicon and aluminium (c) and (d) shows a good correspondence with the inorganic phases around points 5, 6 and 7 in (a) and (b), and presumably arise from the bentonite clay deposited on the surface. Iron distribution in (e) is only concentrated at point 7, and is not observed at points 5 and 6. The cyclic carboxylic anhydride phases observed in Fig. 5(e) can be seen in a point spectrum taken from point 3 (supporting data Fig. S8).

The observation that bentonite is required to generate an active catalyst is supported by the analysis of Sample 2, where the iron-rich regions failed to promote additional dehydration, but rather protected the organic material from additional reactions occurring on the rest of the surface. This is somewhat surprising, since iron is also a common Lewis acid, but is presumably unavailable to act in this way in its oxide form on biochar.

As with Samples 1 and 2, the Raman D–G ratio image of Sample 3 shows a variation in D/G intensity (supporting information, Fig. S7(d)). However, in common with Sample 2, the D/G phases appear to be independent of features in the FTIR, EDX and optical microscopy images. The Raman images show that the mineral components do not change the forms of sp^2 carbon on the surface under our preparation conditions.

3.4. Comparison of biochar models

The main chemical processes in the pyrolysis of lignocellulosic materials are depolymerisation and dehydration [30] resulting in the formation of C=C double bonds, carbonyl, and carboxylic functional groups. The second-derivative FTIR spectra (supporting information, Fig. S9) confirm the chemistry expected from pyrolytic dehydration to produce biochar (Sample 1) from *A. saligna*. Additional dehydration processes are promoted by the oven-drying process used to prepare the mineral enriched samples, and some general observations can be made regarding changes to the *A. saligna* biochar when preparing Samples 2 and 3: a reduced OH peak (~3600 cm^{-1}), and an increased C=C peak (~1600 cm^{-1}), relative to the C=O peak (~1700 cm^{-1}) across all spectra.

XPS provides a quantitative measure of carbon atom types at the surface (<20 nm). The proportion of carbon atoms covalently bound to oxygen on Sample 1 is 20.1%. This increases to 30.8% when heating with iron hydroxide to form Sample 2, and to 28.1% when heating with iron hydroxide-bentonite to form Sample 3. The organic material in Samples 2 and 3 is clearly reacting to acquire more oxygen, but this process is mainly due to torrefaction of the samples, rather than from the presence of mineral additives. The FTIR images demonstrated that the mineral additives do mediate the heat-induced chemical changes in the biochar. In the case of Sample 2, the FTIR images show that the iron oxide retards oxidation of the organic material, while the iron-bentonite in Sample 3 enhances it.

Raman spectroscopy clearly shows a diversity of sp^2 carbon order on all three samples. In Sample 1 the features from the Raman D–G ratio image matched the striations found in the FTIR that resulted from more extensive dehydration during pyrolysis. However the addition of iron hydroxide, and of bentonite-iron hydroxide, did not appear to influence the distribution of the D/G ratio across the sample. The D/G ratios calculated from the averaged Raman spectrum of each sample (Fig. 2 and supporting information Figs. S6 and S10) shows that that the proportion of disordered sp^2 carbon is highest in biochar and decreases when mineral-enriched. However, the features in the Sample 2 and 3 Raman images do not match those seen in the FTIR or EDX, so changes in the D–G ratios are independent of the mineral additives and must be due to heating alone.

A major aim of this study was to demonstrate that laboratory-based FTIR and Raman spectroscopy imaging effectively provides a deeper understanding of the chemical reactions occurring during biochar production, and the distribution of chemical phases on micron and millimetre-scales. The analysis of two mineral-enriched biochar models show that FTIR and Raman imaging, when combined with SEM–EDX imaging, provide new insights into the effect of mineralisation on the organic chemistry of a biochar. These tools provide qualitative information to supplement other quantitative chemical analysis such as XPS and ^{13}C NMR.

4. Conclusion

A combination of reflectance FTIR imaging and SEM–EDX imaging is very effective for characterising the spatial distribution of organic and elemental chemistry on *A. saligna* biochar particles. Images generated from the second-derivative FTIR spectra were found to match features in the SEM, and revealed the formation of millimetre-scale chemical features from differing extents of dehydration during pyrolysis. FTIR imaging enables the spectra to be partitioned into chemical phases to reveal small concentrations of functional groups, such as ketenes, allenes and cyclic anhydrides that would have gone unnoticed in a bulk FTIR analysis. Mineral enrichment of biochar by the addition of iron oxide shows reduced oxidation beneath the iron-rich regions. However, enrichment with bentonite-iron oxide results in increased dehydration/oxidation in the clay-rich regions. The coincidence of these regions strongly supports the idea that aluminium in the clay is acting as a Lewis acid to catalyse dehydration of the organic subsurface. Raman images from D–G ratios in *A. saligna* biochar shows features matching those observed in the FTIR and SEM images. However, the addition of iron oxide and bentonite-iron oxide does not produce new Raman features on biochar.

Appendix A. Supplementary data

Supplementary data associated with this article can be found, in the online version, at http://dx.doi.org/10.1016/j.vibspec.2012.06.006.

References

[1] S. Joseph, M. Camps-Arbestain, Y. Lin, P. Munroe, C.H. Chia, J. Hook, L. van Zwieten, S. Kimber, A. Cowie, B.P. Singh, J. Lehmann, N. Foidl, R. Smernik, J. Amonette, Aust. J. Soil Res. 48 (2010) 501–515.

[2] B.P. Singh, A. Cowie, Carbon and Nutrient Management in Agriculture, Fertilizer and Lime Research Centre Workshop Proceedings, Massey University, Palmerston North, New Zealand, 2008, p. 549.

[3] C. Steiner, W. Teixeira, J. Lehmann, T. Nehls, J.L.V. de Macedo, W. Blum, W. Zech, Plant Soil 291 (2007) 275–290.

[4] Y. Kuzyakov, I. Subbotina, H. Chen, I. Bogomolova, X. Xu, Soil Biol. Biochem. 41 (2009) 210–219.

[5] A. Mukherjee, A.R. Zimmerman, W. Harris, Geoderma 163 (2011) 247–255.

[6] C.H. Chia, P. Munroe, S. Joseph, Y. Lin, Aust. J. Soil Res. 48 (2010) 593–605.

[7] B. Gilbert, J. Banfield, Rev. Mineral. Geochem. 59 (2005) 109–155.

[8] J. Amonette, J. Kim, C. Russell, M. Hendricks, C. Bashore, B. Rieck, ASA-CSSA-SSSA International Annual Meetings, November 12–16, 2006.

[9] P. Ascough, M. Bird, A. Scott, M. Collinson, I. Cohen-Ofri, C. Snape, K. Manquais, J. Archaeol. Sci. 37 (2010) 1590–1599.

[10] M. Keiluweit, P. Nico, M. Johnson, M. Kleber, Environ. Sci. Technol. 44 (2010) 1247–1253.

[11] J. Novak, W. Busscher, D. Watts, D. Laird, M. Ahmedna, M. Niandou, Geoderma 154 (2010) 281–288.

[12] J.H. Yuan, R.K. Xu, H. Zhang, Bioresour. Technol. 102 (2011) 3488–3497.

[13] R. Sharma, J. Wooten, V. Baliga, M. Hajaligol, Fuel 80 (2001) 1825–1836.

[14] K. Yip, M. Xu, C.Z. Li, S.P. Jiang, H. Wu, Energy Fuels 25 (2011) 406–414.

[15] A. Fuertes, M. Camps-Arbestain, M. Sevilla, J. Maciá-Agulló, S. Fiol, R. López, R. Smernik, W. Aitkenhead, F. Arce, F. Macias, Aust. J. Soil Res. 48 (2010) 618–626.

[16] H. Wu, K. Yip, F. Tian, Z. Xie, C.Z. Li, Ind. Eng. Chem. Res. 48 (2009) 10431–10438.

[17] D.J. Gardiner, P.R. Graves, Practical Raman Spectroscopy, Springer-Verlag, Berlin, 1989.

[18] C. Brewer, K. Schmidt-Rohr, J. Satrio, R. Brown, Environmental Progress & Sustainable Energy 28 (2009) 386–396.

[19] Y. Chun, G.Y. Sheng, C.T. Chiou, B.S. Xing, Environ. Sci. Technol. 38 (2004) 4649–4655.

[20] J. Lehmann, B. Liang, D. Solomon, M. Lerotic, F. Luizao, J. Kinyangi, T. Schafer, S. Wirick, C. Jacobsen, Global Biogeochem. Cycles 19 (2005) GB1013, http://dx.doi.org/10.1029/2004GB002435.

[21] R. Salzer, H.W. Siesler, Infrared and Raman Spectroscopic Imaging, Wiley-VCH, Weinheim, 2009.

[22] A. Savitzky, M. Golay, Anal. Chem. 36 (1964) 1627–1639.

[23] M. Guerrero, M.P. Ruiz, A. Millera, M. Alzueta, R. Bilbao, Energy Fuels 22 (2008) 1275–1284.

[24] A. Ferrari, J. Robertson, Phys. Rev. B 61 (2000) 14095.

[25] K.W. Leong, V. Simonte, R. Langer, Macromolecules 20 (1987) 705–712.

[26] M. Back, A. Sehon, Can. J. Chem. 38 (1960) 1261–1270.

[27] G. Socrates, Infrared and Raman Characteristic Group Frequencies—Tables and Charts, 3rd ed., J. Wiley & Sons, Chichester, 2001.

[28] I. Lisovskyy, V. Litovchenko, D. Mazunov, S. Kaschieva, J. Koprinarova, S. Dmitriev, J. Optoelectron. Adv. Mater. 7 (2005) 325–328.

[29] L. Heller-Kallai, T.P. Goldstein, A. Navrotsky, Clays Clay Miner. 44 (1996) 393–397.

[30] J. Lang, Biofuels, Bioprod. Bioref. 1 (2007) 39–48.